

2020-09-23

# WaveStructure Interactions of Flexible Bags with Elastic Tendons: Application to Wave Energy Conversion

Kurniawan, A

<http://hdl.handle.net/10026.1/16160>

---

10.1061/(ASCE)WW.1943-5460.0000607

Journal of Waterway, Port, Coastal and Ocean Engineering

American Society of Civil Engineers

---

*All content in PEARL is protected by copyright law. Author manuscripts are made available in accordance with publisher policies. Please cite only the published version using the details provided on the item record or document. In the absence of an open licence (e.g. Creative Commons), permissions for further reuse of content should be sought from the publisher or author.*

# Wave-Structure Interactions of Flexible Bags with Elastic Tendons

Adi Kurniawan<sup>1</sup>, Scott Brown<sup>2</sup>, David Forehand<sup>3</sup>, and Hugh Wolgamot<sup>4</sup>

<sup>1</sup>Wave Energy Research Centre, The University of Western Australia, 35 Stirling Terrace, Albany  
WA 6330, Australia. Email: adi.kurniawan@uwa.edu.au

<sup>2</sup>School of Engineering, Computing and Mathematics, University of Plymouth, Drake Circus,  
Plymouth, PL4 8AA, United Kingdom

<sup>3</sup>School of Engineering, The University of Edinburgh, Edinburgh, EH9 3JL, United Kingdom

<sup>4</sup>Oceans Graduate School, The University of Western Australia, 35 Stirling Highway, Perth WA  
6009, Australia

## ABSTRACT

A new type of wave energy device has recently been proposed with the key component being a flexible air-filled bag, which is constructed such that the fabric is encased by an array of tendons. The behaviour of the bag in still water under hydrostatic loading and its dynamic response when subjected to hydrodynamic loading in waves were previously analysed using a numerical model developed with the assumption of inextensible tendons. In the present work, the model is extended to include the effects of tendon elasticity. The behaviour of the bag with tendons of various moduli of elasticity is then compared with that of the bag with inextensible tendons. It is found that adding elasticity to the tendons has a similar effect to that of increasing the air volume connected to the bag, that is, it increases the resonance period of the device. Consequently, a bag with elastic tendons can be made even smaller in size than a bag with inextensible tendons in order to match the same target resonance period.

## INTRODUCTION

There are potential advantages in using a flexible deformable body as part of a wave energy device. A flexible device deforms as it oscillates in water, giving rise to a lower hydrostatic stiffness

25 and thus a longer natural period than those of a rigid body of the same size. This allows the size of  
26 the flexible device to be reduced in order to achieve a particular resonance period and, hence, leads  
27 to potential savings in material costs. Flexibility also allows such a device to be tuned to different  
28 environmental conditions through a change in its mean shape, making it much more adaptable than  
29 a rigid device. Transportation of the device is also potentially simpler and cheaper, since the device  
30 can assume its mean shape on-site. Furthermore, a flexible device is expected to be more resilient  
31 to wave impact, enhancing its survivability in extreme conditions.

32 This paper considers a recently proposed wave energy device topology in the form of a com-  
33 pletely sealed system consisting of a flexible air-filled bag connected to a rigid-walled secondary  
34 volume. In the variant that will be discussed here, the device is freely floating and the bag is  
35 surface-piercing (see Fig. 1). As the device heaves in waves, the flexible bag expands and contracts,  
36 forcing two-way exchange of air with the secondary volume. This drives a turbine located between  
37 the two volumes, which acts as a power take-off (PTO). Other variants have also been considered  
38 recently, including a freely floating device with a completely submerged bag (Kurniawan et al.  
39 2017b; Farley 2018) and a bottom-mounted device with either a surface-piercing or a completely  
40 submerged bag (Kurniawan and Greaves 2016).

41 The bag is constructed from a fabric encased by an array of meridional tendons. When inflated,  
42 the fabric forms lobes between the tendons, thus minimising the tension in the fabric while the  
43 tendons become the primary load-carrying elements. The construction is therefore similar to that  
44 used in parachutes (Taylor 1963), underwater lifting bags, super-pressure balloons (Cathey 2009),  
45 and a recently proposed underwater compressed air energy storage system (Pimm et al. 2014).

46 The dynamics of the bag as the device oscillates in water is of interest and has previously been  
47 analysed assuming that the tendons are inextensible (Kurniawan et al. 2017a). Good agreement was  
48 obtained between the numerically predicted response and physical measurements collected from  
49 scaled model tests using bags with relatively stiff tendons, validating the modelling approach.

50 The aim of the present study is to extend this approach to include the effects of tendon elasticity.  
51 Like the previous model, the present model, which will be described in the next section, is linear.

52 As such, the tendons are assumed to obey Hooke's law, whereby the strain of the tendons is linearly  
53 proportional to the applied stress. By simulating tendons of various moduli of elasticity, the impacts  
54 of tendon elasticity on the behaviour of the bag and its performance as a wave energy device will  
55 then be assessed.

## 56 NUMERICAL MODEL

### 57 Static Shape Calculation

58 In contrast to a rigid body, which has a fixed shape, a flexible bag containing a certain amount  
59 of air and ballasted at the bottom will deform as soon as it is immersed in water. The static or  
60 equilibrium shape of the bag in still water is uniquely determined by the internal pressure and  
61 submergence of the bottom of the bag. The method to determine the static shape of the bag follows  
62 that of [Chaplin et al. \(2015a\)](#) and is based on three assumptions: (1) the bag is axisymmetric,  
63 making it sufficient to consider a single tendon; (2) the tension is carried entirely by the tendons  
64 whereas there is no tension in the fabric; (3) the tendons are massless for simplicity.

65 In summary, the process involves discretising the tendon into  $N$  arc elements with known  
66 lengths but unknown radii of curvature. The radius of curvature of each element is obtained by  
67 satisfying the force equilibrium normal to the element, progressing element by element from the  
68 top of the bag to the bottom. As the tendon tension and the top elevation are not known beforehand,  
69 an iterative process is necessary to obtain the correct tension and elevation.

70 A cylindrical coordinate system  $(R, \theta, Z)$  is introduced, where  $Z = 0$  is the mean free surface  
71 and positive  $Z$  points upwards, with the  $Z$ -axis coincident with the vertical axis of the bag. The  
72 tendon is discretized into  $N$  elements of uniform arc length  $h$ , related to its radius of curvature  $\rho_n$   
73 through the relationship

$$74 \quad h = -2\rho_n\phi_n, \quad (1)$$

where  $2\phi_n = \delta A_n$  is the arc sector angle (see Fig. 2). The radius of curvature is defined to be  
positive when the element is bulging outwards. The difference in radial and vertical coordinates

between the ends of the element can then be expressed as

$$\delta R_n = (h/\phi_n) \sin \phi_n \cos(A_n + \phi_n), \quad (2)$$

$$\delta Z_n = (h/\phi_n) \sin \phi_n \sin(A_n + \phi_n), \quad (3)$$

where  $h$  is the arc length of the element including extension. This is calculated using Hooke's law:

$$h = h_0 \left( 1 + \frac{T}{EA} \right), \quad (4)$$

where  $T$  is the sum of tension in all the tendons,  $A$  is the combined cross-sectional area of the tendons,  $E$  is the modulus of elasticity of the tendon, and  $h_0$  is the original length of the tendon before extension. Obviously,  $h \rightarrow h_0$  as  $E \rightarrow \infty$ .

For given internal pressure and submergence of the bag, the procedure begins by making initial guesses for the tension  $T$  and the vertical coordinate at the top of the bag,  $Z_1$ . The value of  $h$  is determined using Eq. (4). Starting from the top of the bag with a first approximation of  $\phi_1 \approx 0$  and working down the tendon, the radius of curvature for each element is calculated using the balance of normal forces

$$\rho_n = \frac{T}{2\pi(P + H_{n+0.5}\rho g Z_{n+0.5})R_{n+0.5}}, \quad (5)$$

where the subscript  $n + 0.5$  denotes the value at the midpoint of element  $n$ ,

$$H_{n+0.5} = \begin{cases} 1, & \text{if } Z_{n+0.5} < 0 \\ 0, & \text{if } Z_{n+0.5} \geq 0, \end{cases} \quad (6)$$

$P$  is the internal bag pressure (relative to atmospheric),  $\rho$  is the water density, and  $g$  is the acceleration due to gravity.

Once the radius of curvature is known for an element, the angle  $\phi_n$  can be evaluated from Eq. (1), allowing a better approximation for  $\delta R_n$  and  $\delta Z_n$  to be obtained using Eqs. (2) and (3). These are then used to obtain better approximations for  $R_{n+0.5}$ ,  $Z_{n+0.5}$ ,  $\rho_n$ , and  $\phi_n$ , which are again

applied in Eqs. (2) and (3) to get the final values of  $\delta R_n$  and  $\delta Z_n$ . The procedure then moves down the tendon to the next element and the above process repeats until the bottom of the bag is reached.

A simple iterative procedure varies the starting values of  $T$  and  $Z_1$  until the last node ( $R_{N+1}, Z_{N+1}$ ) is at the specified radius and submergence to within a small tolerance. For each value of tension, the length of the element is recalculated using Eq. (4).

### Dynamic Model

For the dynamic model, a new set of nodes centred at the elements' midpoints is defined, following the approach of Kurniawan et al. (2017a). In the static shape calculation above, these midpoint nodes are denoted as  $n + 0.5$ , for  $n = 1, \dots, N$ , whereas now they are denoted as  $n = 2, \dots, N'$ , where  $N' = N + 1$ .

The balance of static forces normal to each of these new nodes can be written as

$$2\pi h(P + H_n \rho g Z_n) R_n = T(A_{n-1} - A_n), \quad \text{for } n = 2, \dots, N', \quad (7)$$

which is equivalent to Eq. (5), where Eq. (1) has been used to express the radius of curvature of the element in terms of the angles  $A_{n-1}$  and  $A_n$ . Together with the top ( $n = 1$ ) and bottom ( $n = N' + 1$ ) nodes, there are in total  $N' + 1 = N + 2$  nodes.

For simplicity, only heave and radial motions of the bag will be considered. By expanding the static equation (7) to include time-harmonic motions of small amplitudes about the mean or static position and keeping first-order terms, a set of linearised equations for the dynamic response of node  $n = 2, \dots, N'$  is obtained as

$$2\pi h \left\{ (P + H_n \rho g Z_n) \left( r_n + R_n \frac{\tau}{T + EA} \right) + [p + H_n \rho g (z_n + \xi_3) - p_n^h] R_n \right\} = T(a_{n-1} - a_n) + \tau(A_{n-1} - A_n), \quad (8)$$

where  $r_n$  is the radial displacement of node  $n$ ,  $\tau$  is the change in the total tendon tension,  $p$  is the pressure change in the bag,  $\xi_3$  is the vertical displacement of the substructure,  $z_n$  is the vertical displacement of node  $n$  relative to  $\xi_3$ ,  $a_{n-1}$  and  $a_n$  are the angular displacements of the endpoints

116 of the element, and  $p_n^h$  is the hydrodynamic pressure on node  $n$ . Note that

$$117 \quad h \frac{\tau}{T + EA} = h_0 \frac{\tau}{EA}, \quad (9)$$

118 in accordance with Eq. (4), and so  $h[\tau/(T + EA)]$  is the increase in element length due to  $\tau$ . For  
 119 an inelastic tendon,  $E \rightarrow \infty$ , and the terms proportional to  $1/(T + EA)$  in Eq. (8) vanish.

120 For the substructure, the dynamic equation is not affected by the elasticity of the tendons.  
 121 Therefore,

$$122 \quad -Ta_{N'} \cos A_{N'} - \tau \sin A_{N'} - \pi R_{N'+1}^2 (p + \rho g \xi_3) + f_B^h = -\omega^2 M_B \xi_3, \quad (10)$$

123 as in the inelastic case (Kurniawan et al. 2017a). Here,  $f_B^h$  is the vertical hydrodynamic force on  
 124 the substructure and  $M_B$  is the mass of the substructure.

125 Each of the uppercase quantities in Eqs. (8) and (10), as well as the element length  $h$ , is either  
 126 specified or a solution of the static calculation described earlier, whereas the complex amplitudes  
 127  $p$ ,  $\xi_3$ ,  $\tau$ ,  $f_B^h$ ,  $p_{n|n=2,\dots,N'}^h$ ,  $r_{n|n=1,\dots,N'+1}$ ,  $z_{n|n=1,\dots,N'+1}$ , and  $a_{n|n=1,\dots,N'}$  are as yet unknown. Hence, there  
 128 are  $4N' + 5$  unknowns in total. Equations (8) and (10) together provide  $N'$  equations. In addition,  
 129 the boundary conditions at the top of the bag are  $r_1 = 0$  and  $a_1 = 0$ , whereas at the bottom,  
 130  $r_{N'+1} = z_{N'+1} = 0$ . These are 4 equations altogether. The remaining  $3N' + 1$  equations, which  
 131 will be presented below, are provided through  $N'$  equations relating the angular displacements  
 132 of the elements to the radial displacements of the nodes (Eq. (11));  $N'$  equations relating the  
 133 vertical displacements to the radial displacements of the nodes (Eq. (12));  $N'$  equations relating  
 134 the hydrodynamic pressure  $p_{n|n=2,\dots,N'}^h$  and the hydrodynamic force  $f_B^h$  to the displacements of the  
 135 nodes and the substructure (Eqs. (13) and (14)); and one equation relating the dynamic pressure  $p$   
 136 to the radial and vertical displacements of the nodes (Eq. (15)).

The relationship between the radial and vertical displacements of the nodes, and the angular  
 displacement of the elements can be derived by observing Fig. 3, which is applicable for  $n =$   
 $2, \dots, N' - 1$ . Note that the distance between any two neighbouring nodes at the mean position is  
 $h$ , except for the first two and the last two nodes, where the distance is  $h/2$ . To first order, the two

sets of equations are

$$a_n(Z_{n+1} - Z_n) = (R_{n+1} - R_n) \frac{\tau}{T + EA} - (r_{n+1} - r_n), \quad \text{for } n = 1, \dots, N' \quad (11)$$

$$(R_{n+1} - R_n)(r_{n+1} - r_n) + (Z_{n+1} - Z_n)(z_{n+1} - z_n) = \begin{cases} h^2 \frac{\tau}{T+EA}, & \text{for } n = 2, \dots, N' - 1 \\ \frac{h^2}{4} \frac{\tau}{T+EA}, & \text{for } n = 1 \text{ and } n = N'. \end{cases} \quad (12)$$

The hydrodynamic pressure  $p_n^h|_{n=2, \dots, N'}$  on the nodes and the hydrodynamic force  $f_B^h$  on the substructure can be expressed as the sum of radiation and excitation parts, where the excitation part is the pressure or force due to the incident wave on the mean geometry of the device, whereas the radiation part is due to the device's own motion in otherwise still water. Thus,

$$p_n^h = \begin{cases} 0, & \text{for } n = 2, \dots, n_{wl} - 1 \\ \sum_{k=n_{wl}}^{N'} (-r_k \sin A_{k-0.5} + z_k \cos A_{k-0.5}) p_{n,k}^R + \xi_3 p_{n,3}^R + p_n^{\text{exc}}, & \text{for } n = n_{wl}, \dots, N' \end{cases} \quad (13)$$

$$f_B^h = \sum_{k=n_{wl}}^{N'} (-r_k \sin A_{k-0.5} + z_k \cos A_{k-0.5}) F_{B,k}^R + \xi_3 F_{B,3}^R + F_B^{\text{exc}}. \quad (14)$$

137 Here,  $n = n_{wl}$  is the first node below the waterline;  $-r_k \sin A_{k-0.5} + z_k \cos A_{k-0.5}$  is the outward  
 138 displacement of node  $k$  in the direction normal to the element;  $p_{n,k}^R$  is the pressure on node  $n$  due  
 139 to a unit outward normal displacement of node  $k$ ;  $p_{n,3}^R$  is the pressure on node  $n$  due to a unit  
 140 heave displacement of the mean geometry;  $p_n^{\text{exc}}$  is the excitation pressure on node  $n$ ;  $F_{B,k}^R$  is the  
 141 vertical force on the substructure due to a unit normal displacement of node  $k$ ;  $F_{B,3}^R$  is the vertical  
 142 force on the substructure due to a unit heave displacement of the mean geometry; and  $F_B^{\text{exc}}$  is the  
 143 vertical excitation force on the substructure. The quantities  $p_{n,k}^R$ ,  $p_{n,3}^R$ ,  $p_n^{\text{exc}}$ ,  $F_{B,k}^R$ ,  $F_{B,3}^R$ , and  $F_B^{\text{exc}}$   
 144 can be computed using a radiation/diffraction panel method, such as WAMIT (WAMIT 2016) or  
 145 Nemoh (Babarit and Delhommeau 2015).

146 The dynamic pressure  $p$  in the bag is related to the nodal displacements through (Kurniawan  
 147 et al. 2017a)

$$p = -Ev, \quad (15)$$

with

$$\frac{1}{E} = \frac{V_s C}{\gamma(P + P_{\text{atm}})C + i\omega M_s} + \frac{V}{\gamma(P + P_{\text{atm}})}, \quad (16)$$

$$v = \frac{\pi}{3} \sum_{n=1}^{N'} \left\{ (Z_n - Z_{n+1}) [(2R_n + R_{n+1})r_n + (R_n + 2R_{n+1})r_{n+1}] + (z_n - z_{n+1})(R_n^2 + R_n R_{n+1} + R_{n+1}^2) \right\}. \quad (17)$$

149 In Eq. (16),  $V$  is the mean volume of air connected to the bag (note that  $V$  does not necessarily have  
 150 to be equal to the physical volume of the bag),  $V_s$  and  $M_s$  are the mean volume and mass of air in the  
 151 secondary volume,  $P_{\text{atm}}$  is the atmospheric pressure,  $\gamma$  is the heat capacity ratio, and  $C$  is the PTO  
 152 coefficient, which relates the air mass flow through the PTO and the pressure difference across it:

$$i\omega m_s = -i\omega m = C(p - p_s). \quad (18)$$

154 The dynamic pressure in the secondary volume is given as (Kurniawan et al. 2017a)

$$p_s = \frac{\gamma(P + P_{\text{atm}})C}{\gamma(P + P_{\text{atm}})C + i\omega M_s} P. \quad (19)$$

156 Equation (17) expresses the volume amplitude of the bag  $v$  in terms of the radial and vertical  
 157 displacements of the nodes.

158 Equation (15) thus completes the system of linear equations for the dynamic model. This system  
 159 of equations may be expressed in a matrix form and solved using standard methods.

160 Once the equations are solved, the mean absorbed power can be obtained from

$$\mathcal{P} = \frac{C}{2\rho_{\text{air}}} |p - p_s|^2, \quad (20)$$

162 where  $\rho_{\text{air}}$  is the mass density of air in the system at the mean pressure  $P$ . For convenience, we

163 may introduce the PTO damping  $B_{\text{PTO}}$ , defined as

$$164 \quad B_{\text{PTO}} = \rho_{\text{air}}/C, \quad (21)$$

165 from which we have an alternative expression for the mean absorbed power:

$$166 \quad \mathcal{P} = \frac{|p - p_s|^2}{2B_{\text{PTO}}}. \quad (22)$$

## 167 **STATIC BEHAVIOUR**

168 At equilibrium, the weight of a freely floating body equals its buoyancy. This means that for  
169 a given amount of ballast, the submergence and shape of the bag must be such that they give the  
170 required buoyancy. For the same amount of ballast, the submergence and shape vary, depending  
171 on the amount of air in the bag. Plotting these as a function of the bag pressure gives C-shaped  
172 trajectories, as first reported by [Chaplin et al. \(2015b\)](#) for a bag with inextensible tendons.

173 As an example, let us consider a bag with an initial tendon length of 0.95 m, bottom radius  
174  $R_{N+1}$  of 0.07 m, and required buoyancy of 0.1 m<sup>3</sup> of water, that is, we use the same dimensions as  
175 used by [Kurniawan et al. \(2017a\)](#) for a model-scale bag. Fig. 4 shows trajectories of the top and  
176 bottom elevations of the bag for various values of  $EA$ , ranging from 5 kN to 1 GN. The 1 GN case  
177 may be considered as inextensible. Each trajectory is obtained by calculating the static shape of the  
178 bag for a range of internal pressure and bottom elevation, and finding those shapes which give the  
179 required buoyancy. In general, the trajectories are C-shaped, but it may be noticed that they exhibit  
180 a reversed curvature along the upper end as elasticity is increased. Each trajectory pair traces the  
181 top and bottom elevations of the bag at equilibrium, as the amount of air in the bag is varied. With  
182 decreasing amount of air, the internal pressure first decreases until it reaches a minimum, and then  
183 increases as the bag sits lower in the water, before it sinks when there is not enough air to keep the  
184 bag afloat. Similar trajectories can be plotted for the radius of the bag at the water plane, the total  
185 tension in all tendons, and the volume of the bag. These are shown in Fig. 5.

186 All trajectories in these figures shift to the left as the tendon elasticity is increased. This is

187 because a bag with more elastic tendons can expand more and thus accommodate more air without  
188 as much increase in pressure than a bag with stiffer tendons can, as seen from Fig. 5(c). It is also  
189 observed that the behaviour of the bags with various tendon elasticity is more similar to each other  
190 when they are almost fully deflated than when they are fully inflated (the trajectories merge into one  
191 line). As seen from Fig. 5(b), the total tension in the tendons tends asymptotically to approximately  
192 1 kN with decreasing amount of air, irrespective of the value of  $EA$ . This is due to the fact that  
193 with decreasing amount of air, all bags will have an increasingly elongated profile in the vertical  
194 direction, and thus the tendons will be more vertically aligned. The sum of tension in the tendons  
195 will then be approximately equal to the submerged weight of the substructure, which in this case is  
196 equal to 100 kgf or 0.981 kN. A similar observation can be made from Fig. 5(c). The volumes of  
197 the bags all tend to  $0.1 \text{ m}^3$ , their required buoyancy, when they are just about to sink.

198 Fig. 6(a) shows the tendon profiles at the minimum pressures possible with different values of  
199  $EA$ . Plotting the top and bottom elevations of the bag against the minimum possible bag pressures  
200 for the different values of  $EA$  reveals approximately linear relationships between the elevations and  
201 the minimum possible pressure, as evident from Fig. 6(b).

## 202 **DYNAMIC BEHAVIOUR**

203 For the dynamic calculations, it is assumed that the substructure is a cylinder with a hemispher-  
204 ical base (as in Fig. 1 and 8). The cylinder radius is 0.152 m and the cylinder height, excluding the  
205 hemisphere, is 0.460 m. The mass of the substructure is 140 kg. The same dimensions were used  
206 in the previous study (Kurniawan et al. 2017a). The air density at atmospheric pressure is given as  
207  $1.225 \text{ kg/m}^3$ , while the heat capacity ratio is taken as 1.4. For the calculation of the hydrodynamic  
208 quantities, the water depth is assumed to be 3 m. In the calculations, the tendon is discretised into  
209 40 elements, i.e.,  $N = 40$ .

210 Four cases are defined having different tendon elasticity but with equilibrium conditions selected  
211 such that the bags all have the same waterplane radius of 0.341 m at mean position, to provide  
212 an equitable comparison. The cases are defined in Table 1, where the mean bag pressure and bag  
213 bottom elevation obtained from the static calculations are given, as well as the calculated mean

214 bag volume, tendon tension, and element length. A high value of  $EA$  is chosen for Case 1 and  
215 thus it can be regarded to approximate a bag with inextensible tendons. The mean tendon profiles  
216 corresponding to these four cases are shown in Fig. 7.

217 The volume of air connected to the bag,  $V$ , is taken to be equal to the physical volume of the  
218 bag. This varies slightly depending on the mean shape of the bag. The secondary air volume,  $V_s$ ,  
219 is kept at  $2.268 \text{ m}^3$ . Although this is much bigger than the volume of the device at model scale, the  
220 corresponding full-scale total volume of air ( $V + V_s$ ) would fit into a full-scale device, due to the  
221 scaling effects associated with air compressibility (Chaplin et al. 2015a).

222 Typical responses of the device are shown in Fig 8, which displays snapshots of the device  
223 during one oscillation cycle, when subjected to incident waves of amplitude 0.05 m and various  
224 periods (as indicated above each plot). These periods correspond to the periods at which the  
225 power function (i.e., the mean absorbed power divided by the incident wave amplitude squared; see  
226 Eq. (20) and Eq. (22)) peaks in each case, where the same PTO damping,  $B_{\text{PTO}} = 15.58 \text{ kPa m}^{-3}$   
227 s, has been used for all cases.

228 The response of the device varies depending on the selected PTO damping. To illustrate this,  
229 each of the dynamic responses in Fig. 9 is plotted for a range of different PTO damping values.  
230 Greater PTO damping (or, smaller PTO coefficient  $C$ ) corresponds to greater resistance of the flow  
231 between the two volumes; cf. Eq. (18). Fig. 9 shows that as the PTO damping is decreased (i.e.,  
232 the flow resistance is reduced), the peak of the response shifts from left to right, i.e., the device  
233 resonates at longer periods. This is because the two volumes increasingly become one volume as  
234 the flow resistance is reduced, resulting in a greater compliance of the bag which leads to longer  
235 resonance periods. This effect is clearly seen from the plots of the pressure amplitudes, Fig. 9(b),  
236 where the pressures in the two volumes become more equal as the flow resistance is reduced. This  
237 peak shifting, which results in a double-peaked response envelope, appears to be a characteristic of  
238 compressible devices with two air volumes (Kurniawan et al. 2014).

239 For comparison, the responses of a rigid body having the same geometry as the mean geometry  
240 of the bag and absorbing energy through heave relative to a fixed reference (e.g. the sea bed) are

241 also plotted in Fig. 9(a) and (e). The PTO damping in each case is chosen to maximise the absorbed  
242 power at resonance, and they are equal to 81.84, 84.66, 89.49, and 92.46 kg/s for Case 1 to 4. The  
243 envelopes of the power function for the rigid body are also shown in Fig. 9(a). Since the mean  
244 geometries of the bag are similar, and they have the same waterplane radius and mass, the rigid  
245 bodies have similar responses. This, however, is not the case with the flexible bags. The elasticity  
246 of the tendons has a clear effect on the dynamic response of the bag, with the more elastic bags  
247 resonating at longer periods and with generally higher amplitudes.

248 As seen from Fig. 9(a), the rigid body has a broader power function envelope due to the fact  
249 that it is reacting against a fixed reference. The bandwidth of the flexible bag device is narrower  
250 because, firstly, it is a self-reacting device and, secondly, it is deformable. The flexible bag device  
251 can however attain higher values of mean absorbed power at the peaks.

252 The change in tendon element length per incident wave amplitude is plotted in Figure 10 for  
253 Cases 1 to 4. The curves in this figure are proportional to the tension amplitude curves in Fig. 9(d)  
254 by a factor of  $EA$ . With increasing elasticity, there is more stretch in the tendons.

255 A possible disadvantage of having too high elasticity is the higher strain which may limit the  
256 range of wave conditions in which the device is stable. This may be inferred from the static  
257 trajectories in Fig. 4, where it is seen that with increasing elasticity, the C-shaped trajectories  
258 become more elongated vertically, implying that the device becomes increasingly more sensitive to  
259 small variations in the amount of air in the system and thus it would be more difficult to maintain  
260 equilibrium.

## 261 **PERFORMANCE IN AN ACTUAL WAVE CLIMATE**

262 A longer resonance period is beneficial in terms of device economy. Adding elasticity to the  
263 tendons increases the resonance period of the body, and therefore allows the device to be made even  
264 smaller. In this section, the performance of a full-scale flexible bag device with various tendon  
265 elasticity in an actual wave climate is compared. The chosen wave climate is that of the European  
266 Marine Energy Centre (EMEC) in Scotland. The joint probability diagram for significant wave  
267 height and mean wave period at this location is taken from (Nielsen and Pontes 2010).

The calculation assumes that each sea state is described by the modified Pierson-Moskowitz spectrum (Tucker and Pitt 2001), and, for simplicity, the following approximate relationships between the peak period  $T_p$ , mean period  $T_z$ , and energy period  $T_e$  are assumed (Nielsen and Pontes 2010):

$$T_p = 1.4 T_z, \quad (23)$$

$$T_e = 1.2 T_z. \quad (24)$$

268 For each sea state, the mean absorbed power is calculated as

$$269 \quad \mathcal{P}(H_s, T_z) = 2 \int_0^\infty \frac{\mathcal{P}(\omega)}{|\eta|^2} S(\omega, H_s, T_z) d\omega, \quad (25)$$

270 where  $S(\omega, H_s, T_z)$  is the wave spectrum for the sea state. Two cases are considered. First, the PTO  
 271 damping is assumed to be constant and optimised to maximise the mean absorbed power for the  
 272 entire wave climate, which is given as

$$273 \quad \bar{\mathcal{P}} = \sum_{H_s} \sum_{T_z} \mathcal{P}(H_s, T_z) \text{Prob}(H_s, T_z), \quad (26)$$

274 where  $\text{Prob}(H_s, T_z)$  is the long-term probability of occurrence of the sea state. Second, the PTO  
 275 damping is optimised to maximise the mean absorbed power for each sea state.

276 The mean absorbed power for the given wave climate is calculated for a number of different  
 277 scales of the device. From this, the mean capture width ratio can be calculated according to

$$278 \quad \overline{\text{CWR}} = \bar{\mathcal{P}} / \bar{J}, \quad (27)$$

279 where

$$280 \quad \bar{J} = \sum_{H_s} \sum_{T_z} \frac{\rho g^2}{64\pi} T_e H_s^2 \text{Prob}(H_s, T_z), \quad (28)$$

281 assuming deep water condition, for simplicity.

282 The mean capture width ratio  $\overline{CWR}$  as a function of scale is plotted in Fig. 11(a) for the four  
283 tendon elasticity cases defined earlier. The mean capture width ratio is seen to increase with scale,  
284 in agreement with the observation made by (Babarit 2015). As expected, the device in Case 4  
285 (which has the most elastic tendons) has the highest  $\overline{CWR}$  for a given scale, up to approximately  
286 a scale of 30, where the  $\overline{CWR}$  appears to peak. The  $\overline{CWR}$  for devices in Cases 1 to 3 increase  
287 further beyond this scale and appear to peak at a larger scale. Using a constant PTO damping for  
288 the entire wave climate is seen to produce almost the same performance as using variable PTO  
289 damping optimised for each sea state.

290 The growth of the  $\overline{CWR}$  with scale (up to a saturation point which happens at a relative  
291 large scale) makes sense if we consider that the wave energy resource for a particular sea state is  
292 proportional to wave period and to the square of the wave height (see Eq. (28)). So, although the  
293 most frequently occurring sea states are composed of relatively short waves, the waves with the  
294 highest average energy over the entire wave climate are longer. These longer waves therefore have  
295 more weighting in the total energy production and, consequently, larger devices are preferred.

296 For the same wave climate, the mean absorbed power is proportional to the  $\overline{CWR}$  times the  
297 scale. If cost were linearly proportional to scale, then the  $\overline{CWR}$  would be a true representation of  
298 the device economy, and a device would need to be sized to a scale where the  $\overline{CWR}$  is maximum.  
299 At a scale of 30, this would be quite a large device.

300 A completely different picture is obtained if, instead, the mass of the device is taken as a proxy  
301 for cost, as shown in Fig. 11(b), where the ratio of the mean absorbed power to device mass (or  
302 ballast mass if the mass of the bag is neglected, as done here) is plotted for the four cases. Again,  
303 the device with the highest tendon elasticity has the highest power-to-mass ratio. However, it is  
304 more beneficial to have a smaller device, with the power-to-mass ratio peaking at a scale smaller  
305 than 10.

306 Taking the device mass as a proxy for cost is just one among many possibilities. The actual cost  
307 of the device may be proportional to (scale)<sup>2</sup> or somewhere between (scale)<sup>1</sup> and (scale)<sup>3</sup>, rather  
308 than (scale)<sup>3</sup>, as implied in taking mass as a proxy for cost.

309 It should be noted that to maximise power absorption, especially for a relatively small device,  
310 requires displacement amplitudes that can be exceedingly large. Fig. 12 shows the ratio of the  
311 maximum standard deviation of the bag top displacement to the mean freeboard. To attain the  
312 absorbed power values shown in Fig. 11 would require a device of a scale smaller than 20 to be  
313 completely submerged.

314 The preceding analysis applies for a passive device without any means for reactive control.  
315 A different conclusion may be obtained if reactive control is considered. In addition, the PTO  
316 damping has been allowed to assume any value, and no drag has been included in the model.

## 317 **CONCLUSION**

318 Static and dynamic numerical analyses of a wave energy device incorporating a flexible bag with  
319 elastic tendons have been presented. Linear analysis has been employed throughout and only heave  
320 and radial displacements have been considered. From the static analysis, it is found that adding  
321 elasticity to the tendons lowers the minimum possible pressure in the bag. C-shaped trajectories  
322 similar to those of a bag with inextensible tendons are also found with the elastic-tendon bag, but  
323 the trajectories are characterised by steeper gradients as the elasticity is increased.

324 Dynamically, the effect of having elastic tendons is found to be similar to that of having a larger  
325 air volume connected to the bag. An elastic-tendon bag has an even longer resonance period than  
326 an inextensible-tendon bag for the same waterplane area and the same amount of ballast, offering  
327 a greater potential for cost saving. Calculations of the expected absorbed power in an actual wave  
328 climate have been performed confirming the benefit, in terms of power production, of having elastic  
329 tendons over inextensible tendons.

330 Varying the PTO damping (i.e., the flow resistance between the two air volumes) shifts the  
331 peak response of the flexible bag device across a range of periods, with a resulting double-peaked  
332 envelope of the mean absorbed power. The multi-peak envelope is similar to that of a classical  
333 self-reacting point absorber composed of two rigid bodies (Falnes 1999). However, whereas the  
334 response of the two-body device alternates between single-peaked (when the PTO damping is  
335 large) and double-peaked (when the PTO damping is small), the response of the flexible bag device

336 stays single-peaked but shifts from shorter to longer periods as the PTO damping is reduced. A  
337 more detailed comparison with a classical self-reacting point absorber, including calculations of  
338 the expected power production in an actual wave climate, is planned for a future study.

## 339 **ACKNOWLEDGMENTS**

340 Dr. Thanh Toan Tran from the National Renewable Energy Laboratory (NREL) provided the  
341 hydrodynamic coefficients for the dynamic response calculations. A.K. is supported by the Wave  
342 Energy Research Centre, jointly funded by The University of Western Australia and the West-  
343 ern Australian Government, via the Department of Primary Industries and Regional Development  
344 (DPIRD). Part of this study was conducted while A.K. was with the Department of Civil Engi-  
345 neering, Aalborg University. S.B. and D.F would also like to acknowledge support from the Wave  
346 Energy Scotland through the project “A feasibility study on Elastomeric-based WECs” (ELASTO).

## 347 **REFERENCES**

- 348 Babarit, A. (2015). “A database of capture width ratio of wave energy converters.” *Renewable*  
349 *Energy*, 80, 610–628.
- 350 Babarit, A. and Delhommeau, G. (2015). “Theoretical and numerical aspects of the open source  
351 BEM solver NEMOH.” *Proceedings of the 11th European Wave and Tidal Energy Conference*  
352 *(EWTEC2015)*, Nantes, France.
- 353 Cathey, H. (2009). “The NASA super pressure balloon – A path to flight.” *Advances in Space*  
354 *Research*, 44(1), 23–38.
- 355 Chaplin, J., Farley, F., Greaves, D., Hann, M., Kurniawan, A., and Cox, M. (2015a). “Numerical  
356 and experimental investigation of wave energy devices with inflated bags.” *Proc. 11th Eur. Wave*  
357 *and Tidal Energy Conf. Nantes, France*.
- 358 Chaplin, J. R., Farley, F., Kurniawan, A., Greaves, D., and Hann, M. (2015b). “Forced heaving  
359 motion of a floating air-filled bag.” *Proc. 30th Int. Workshop on Water Waves and Floating*  
360 *Bodies*, Bristol, UK.
- 361 Falnes, J. (1999). “Wave-energy conversion through relative motion between two single-mode  
362 oscillating bodies.” *Journal of Offshore Mechanics and Arctic Engineering*, 121, 32–38.

363 Farley, F. J. M. (2018). “The underwater resonant airbag: a new wave energy converter.” *Pro-*  
364 *ceedings of the Royal Society A: Mathematical, Physical and Engineering Sciences*, 474(2215),  
365 20170192.

366 Kurniawan, A., Chaplin, J. R., Greaves, D. M., and Hann, M. (2017a). “Wave energy absorption  
367 by a floating air bag.” *Journal of Fluid Mechanics*, 812, 294–320.

368 Kurniawan, A., Chaplin, J. R., Hann, M. R., Greaves, D. M., and Farley, F. J. M. (2017b). “Wave  
369 energy absorption by a submerged air bag connected to a rigid float.” *Proceedings of the Royal*  
370 *Society A: Mathematical, Physical and Engineering Sciences*, 473(2200), 20160861.

371 Kurniawan, A. and Greaves, D. (2016). “Wave power absorption by a submerged balloon fixed to  
372 the sea bed.” *IET Renewable Power Generation*, 10, 1461–1467(6).

373 Kurniawan, A., Greaves, D., and Chaplin, J. (2014). “Wave energy devices with compressible  
374 volumes.” *Proceedings of the Royal Society of London A*, 470(2172).

375 Nielsen, K. and Pontes, T. (2010). “Annex II Task 1.1 Generic and site-related wave energy data.”  
376 *Report No. T02-1.1*, OES IA (September).

377 Pimm, A. J., Garvey, S. D., and de Jong, M. (2014). “Design and testing of energy bags for  
378 underwater compressed air energy storage.” *Energy*, 66, 496–508.

379 Taylor, G. I. (1963). “On the shapes of parachutes.” *The Scientific Papers of G. I. Taylor*, G. K.  
380 Batchelor, ed., Cambridge University Press, 26–37. (Original work published 1919).

381 Tucker, M. J. and Pitt, E. G. (2001). *Waves in Ocean Engineering*, Vol. 5 of *Ocean Engineering*  
382 *Series*. Elsevier.

383 WAMIT (2016). *User Manual*. WAMIT, Inc., Chestnut Hill, MA, <<http://www.wamit.com>>. Ver-  
384 sion 7.2.

385 **List of Tables**

386 1 Parameters of the selected cases . . . . . 19

**TABLE 1.** Parameters of the selected cases

Case	$EA$ [N]	$P$ [m]	$Z_{N'+1}$ [m]	$V$ [m <sup>3</sup> ]	$T$ [N]	$h$ [m]
1	$1 \times 10^9$	0.370	-0.438	0.141	$1.375 \times 10^3$	$2.375 \times 10^{-2}$
2	$5 \times 10^4$	0.328	-0.467	0.142	$1.210 \times 10^3$	$2.432 \times 10^{-2}$
3	$1 \times 10^4$	0.274	-0.547	0.145	$0.997 \times 10^3$	$2.612 \times 10^{-2}$
4	$5 \times 10^3$	0.256	-0.630	0.147	$0.927 \times 10^3$	$2.816 \times 10^{-2}$

387  
388  
389  
390  
391  
392  
393  
394  
395  
396  
397  
398  
399  
400  
401  
402  
403  
404  
405  
406  
407

## List of Figures

1	Sketch of the floating bag device, showing the main components and the two air volumes, $V$ and $V_s$ . . . . .	22
2	One arc element. . . . .	23
3	Positions of two neighbouring nodes before and after displacements. . . . .	24
4	Trajectories of top and bottom elevations of the bag for various values of $EA$ : from left to right, 5 kN, 7 kN, 10 kN, 20 kN, 50 kN, 1 GN. The bag pressure is measured in terms of the pressure head (i.e., $P/(\rho g)$ ). . . . .	25
5	Trajectories of (a) waterplane radius of the bag, (b) total tendon tension, and (c) bag volume for various values of $EA$ : from left to right, 5 kN, 7 kN, 10 kN, 20 kN, 50 kN, 1 GN. . . . .	26
6	(a) Tendon profiles at the minimum bag pressures possible with various values of $EA$ : highest profile to lowest profile, 5 kN, 7 kN, 10 kN, 20 kN, 50 kN, 1 GN. (b) Variations of top and bottom elevations of the bag with minimum possible bag pressures for various values of $EA$ . . . . .	27
7	Mean tendon profiles having the same waterplane radius of 0.341 m: Case 1 (solid), Case 2 (dashed), Case 3 (dotted), and Case 4 (dash-dotted). . . . .	28
8	Snapshots of the device at mean position (thick line) and when the top of the bag is at its highest and lowest elevations (thin lines). The oscillations are in response to incident waves of amplitude 0.05 m and with periods as indicated. The PTO damping, $B_{PTO} = 15.58 \text{ kPa m}^{-3} \text{ s}$ , is kept constant in all cases. . . . .	29

408 9 (a) Power function, (b) dynamic pressure per incident wave amplitude, (c) bag  
409 volume change per incident wave amplitude, (d) tension amplitude per incident  
410 wave amplitude, and (e) response amplitude operator of the top of the bag, for  
411 Cases 1 to 4. In (a)–(e), solid lines are responses obtained with four different  
412 PTO damping values: 112.60, 42.10, 15.58, and 5.74 kPa m<sup>-3</sup> s. As these values  
413 increase, so the response peaks shift from left to right. The same set of PTO  
414 damping values is used for each case. In (b), black lines are the pressure in the  
415 bag, whereas grey lines are the pressure in the secondary volume. In (a) and  
416 (e), dashed line is the response of a rigid body of the same geometry, with PTO  
417 damping selected to maximise the mean absorbed power at resonance (solid) and  
418 PTO damping optimised at every period (grey). In (a), grey thick line is the  
419 envelope of the black solid lines for all PTO coefficients (not just the four shown  
420 here). . . . . 30

421 10 Change in element length per incident wave amplitude, for Cases 1 to 4. . . . . 31

422 11 (a) Mean capture width ratio and (b) mean absorbed power per unit mass (in  
423 kW/ton), plotted as functions of device scale, for the four tendon elasticity cases:  
424 Case 1 (solid), Case 2 (dashed), Case 3 (dotted), and Case 4 (dash-dotted). Left  
425 column is for constant PTO damping optimised to maximise mean absorbed power  
426 for the entire wave climate, whereas right column is for PTO damping optimised  
427 to maximise the mean absorbed power for each sea state. . . . . 32

428 12 Maximum standard deviation of the displacement of the bag top, normalised with  
429 the mean freeboard, for the four tendon elasticity cases: Case 1 (solid), Case 2  
430 (dashed), Case 3 (dotted), and Case 4 (dash-dotted). . . . . 33

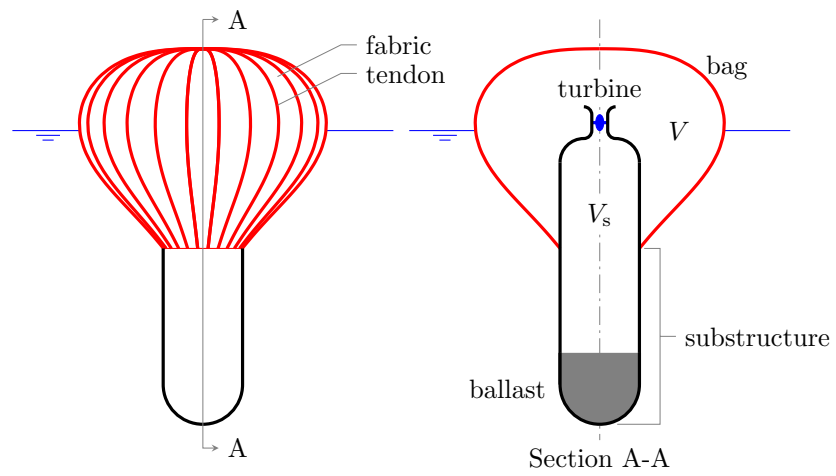


**Fig. 1.** Sketch of the floating bag device, showing the main components and the two air volumes,  $V$  and  $V_s$ .

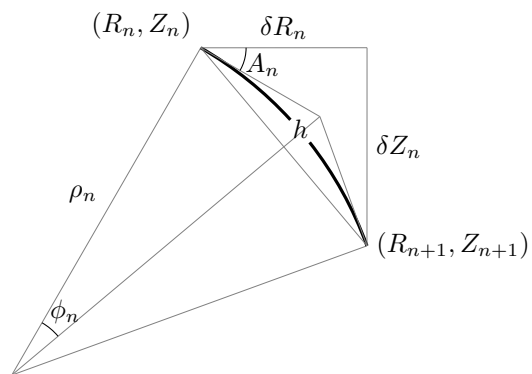


**Fig. 2.** One arc element.

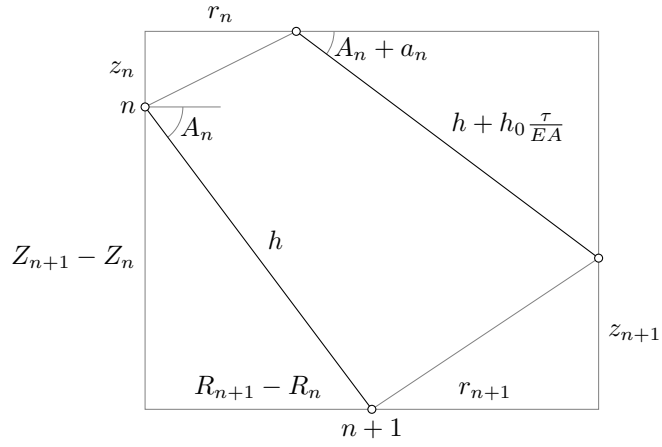


**Fig. 3.** Positions of two neighbouring nodes before and after displacements.

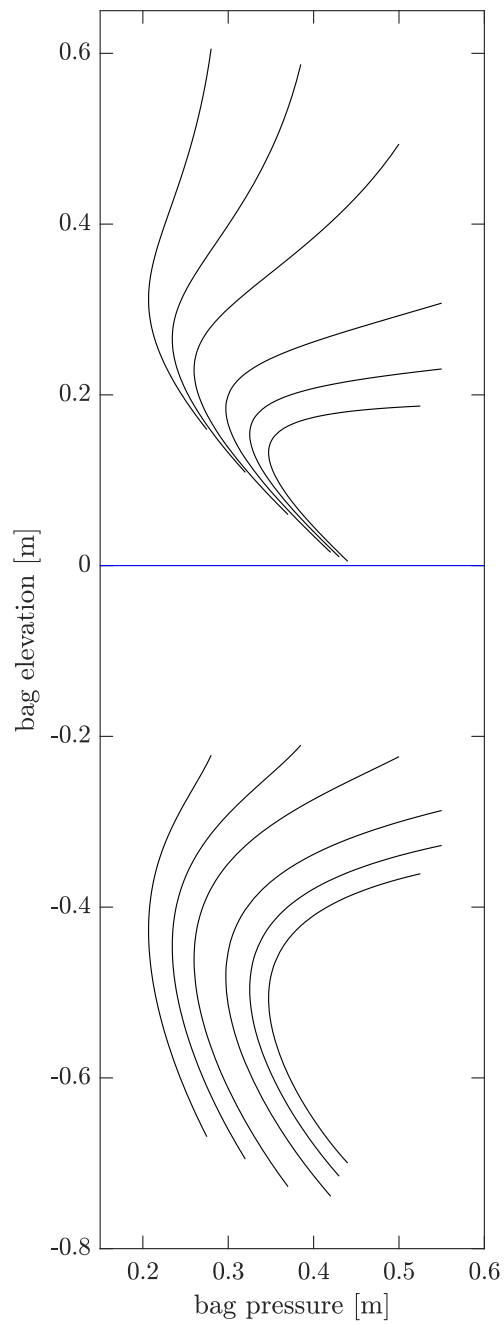


**Fig. 4.** Trajectories of top and bottom elevations of the bag for various values of  $EA$ : from left to right, 5 kN, 7 kN, 10 kN, 20 kN, 50 kN, 1 GN. The bag pressure is measured in terms of the pressure head (i.e.,  $P/(\rho g)$ ).

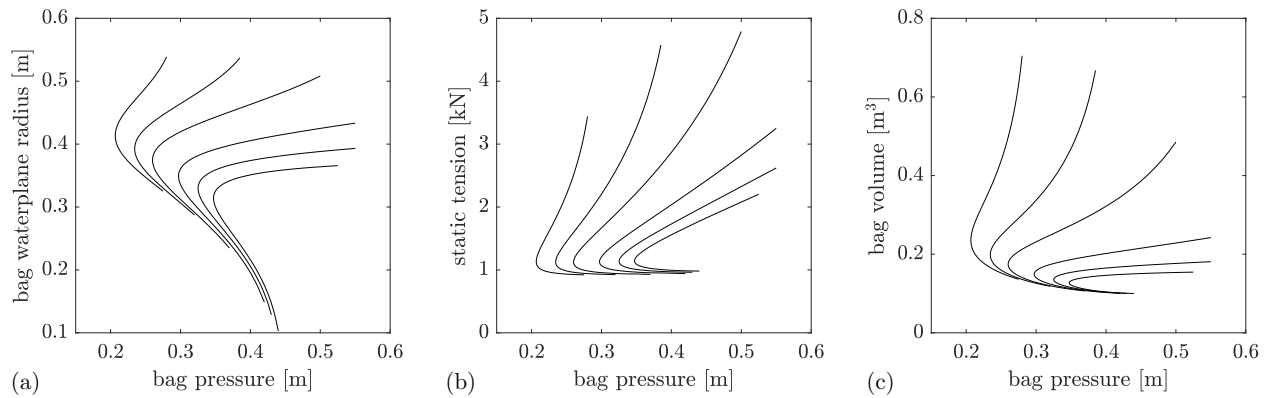


**Fig. 5.** Trajectories of (a) waterplane radius of the bag, (b) total tendon tension, and (c) bag volume for various values of  $EA$ : from left to right, 5 kN, 7 kN, 10 kN, 20 kN, 50 kN, 1 GN.

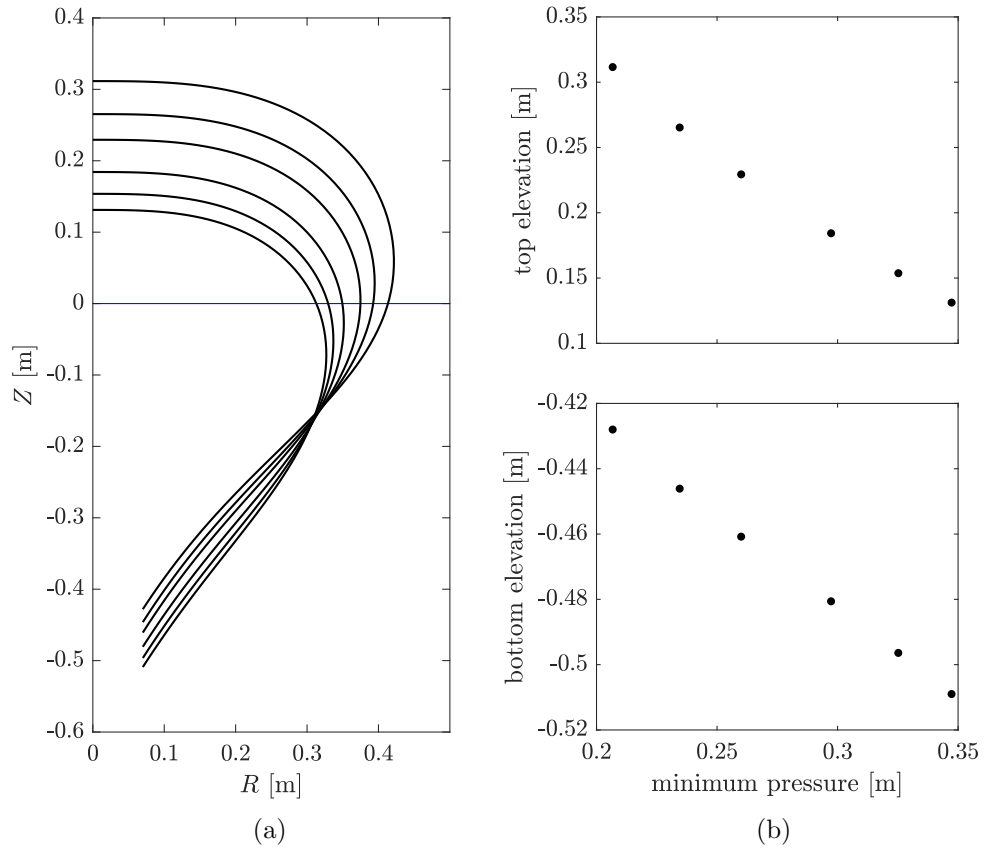


**Fig. 6.** (a) Tendon profiles at the minimum bag pressures possible with various values of  $EA$ : highest profile to lowest profile, 5 kN, 7 kN, 10 kN, 20 kN, 50 kN, 1 GN. (b) Variations of top and bottom elevations of the bag with minimum possible bag pressures for various values of  $EA$ .

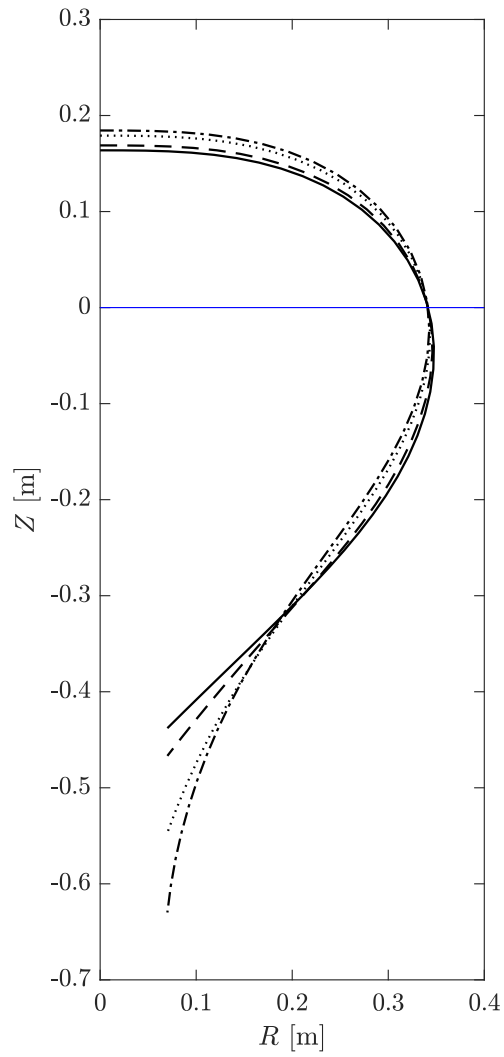


**Fig. 7.** Mean tendon profiles having the same waterplane radius of 0.341 m: Case 1 (solid), Case 2 (dashed), Case 3 (dotted), and Case 4 (dash-dotted).

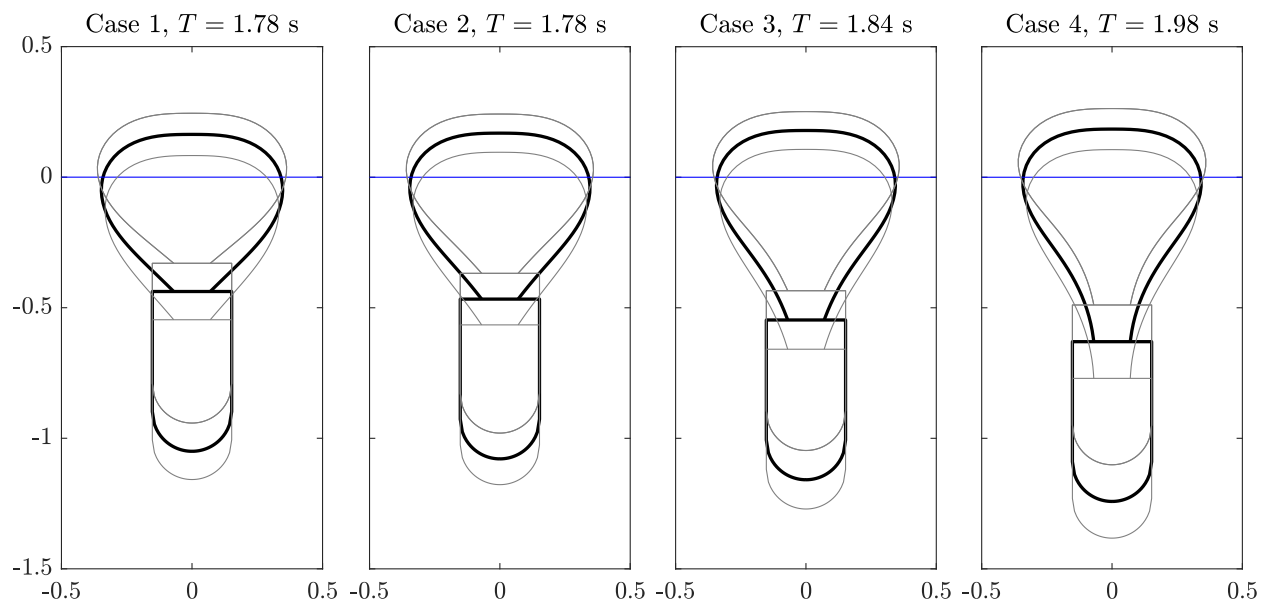


**Fig. 8.** Snapshots of the device at mean position (thick line) and when the top of the bag is at its highest and lowest elevations (thin lines). The oscillations are in response to incident waves of amplitude 0.05 m and with periods as indicated. The PTO damping,  $B_{PTO} = 15.58 \text{ kPa m}^{-3} \text{ s}$ , is kept constant in all cases.

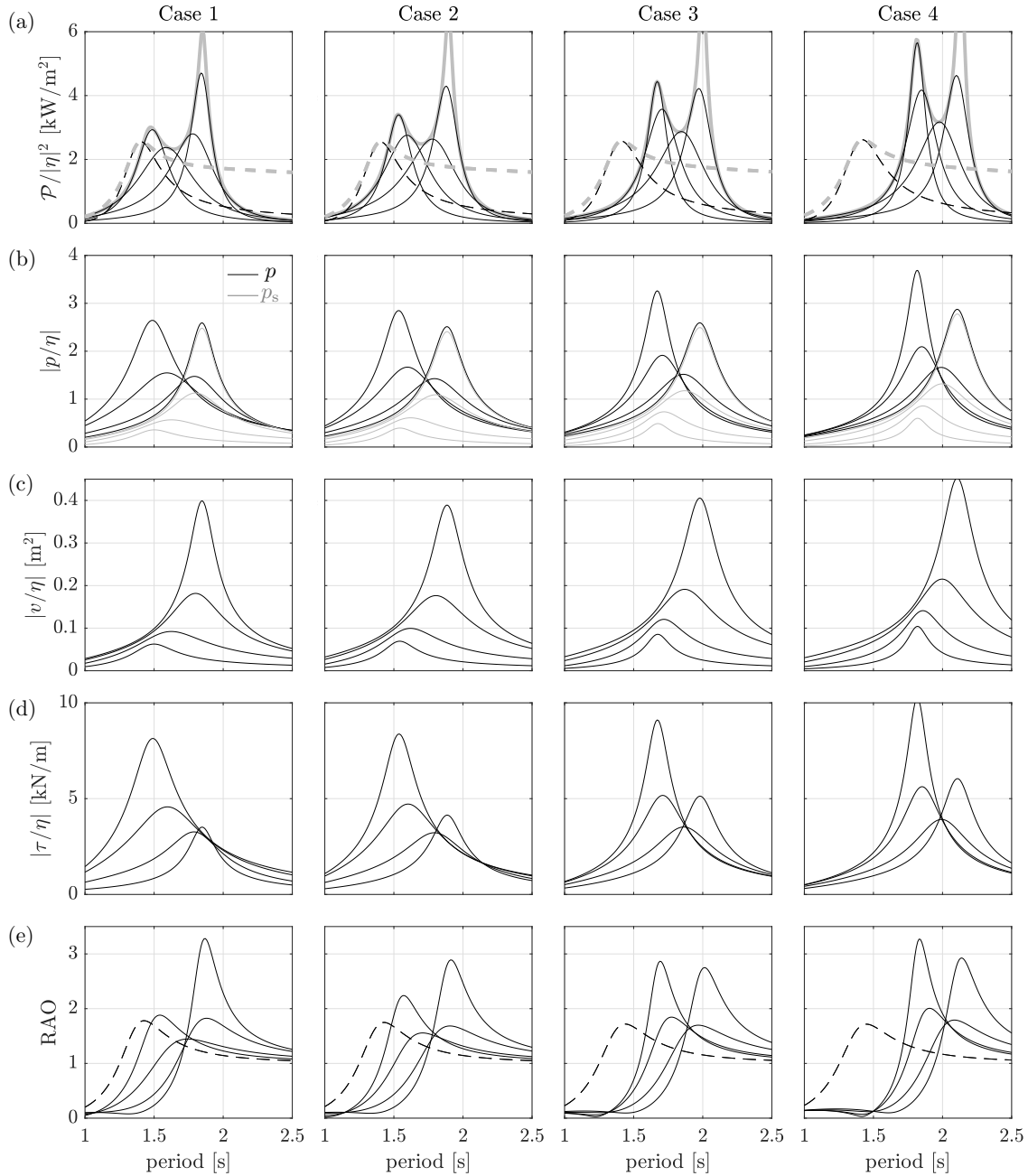


**Fig. 9.** (a) Power function, (b) dynamic pressure per incident wave amplitude, (c) bag volume change per incident wave amplitude, (d) tension amplitude per incident wave amplitude, and (e) response amplitude operator of the top of the bag, for Cases 1 to 4. In (a)–(e), solid lines are responses obtained with four different PTO damping values: 112.60, 42.10, 15.58, and 5.74 kPa m<sup>-3</sup> s. As these values increase, so the response peaks shift from left to right. The same set of PTO damping values is used for each case. In (b), black lines are the pressure in the bag, whereas grey lines are the pressure in the secondary volume. In (a) and (e), dashed line is the response of a rigid body of the same geometry, with PTO damping selected to maximise the mean absorbed power at resonance (solid) and PTO damping optimised at every period (grey). In (a), grey thick line is the envelope of the black solid lines for all PTO coefficients (not just the four shown here).

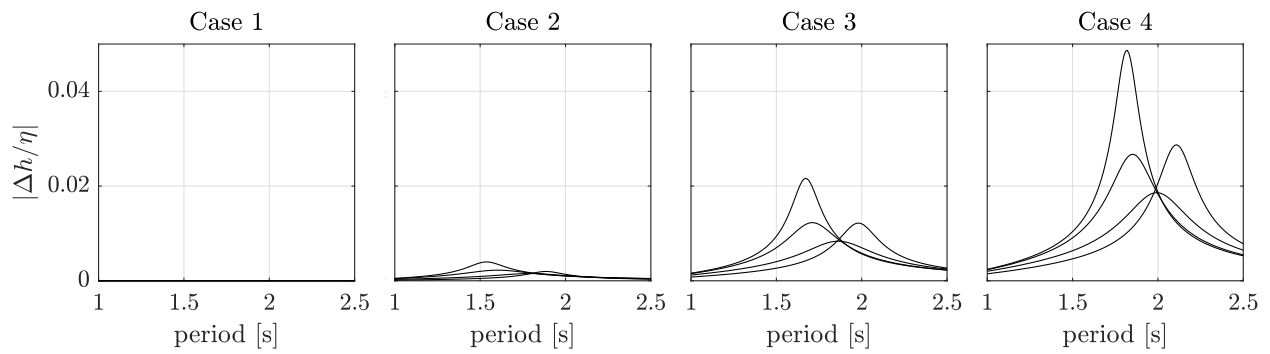


**Fig. 10.** Change in element length per incident wave amplitude, for Cases 1 to 4.

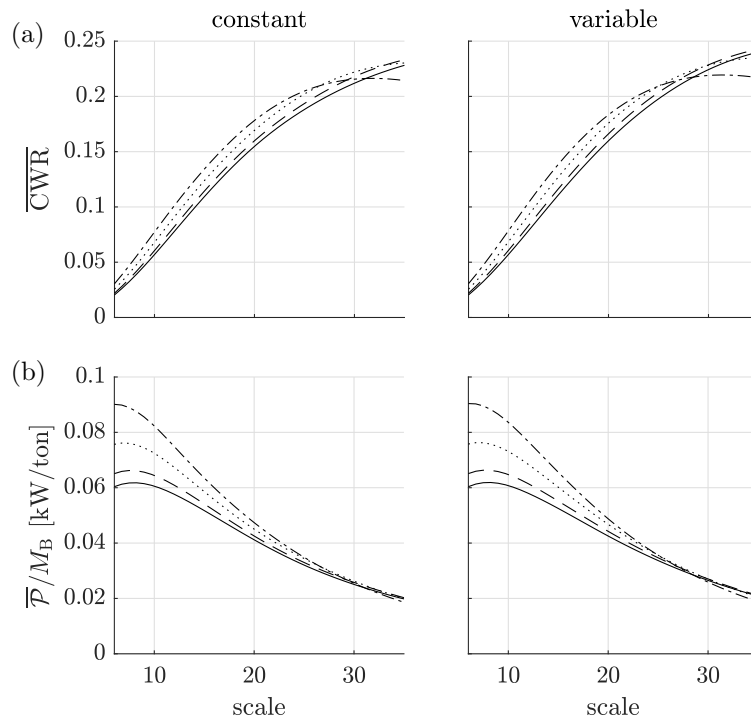


**Fig. 11.** (a) Mean capture width ratio and (b) mean absorbed power per unit mass (in kW/ton), plotted as functions of device scale, for the four tendon elasticity cases: Case 1 (solid), Case 2 (dashed), Case 3 (dotted), and Case 4 (dash-dotted). Left column is for constant PTO damping optimised to maximise mean absorbed power for the entire wave climate, whereas right column is for PTO damping optimised to maximise the mean absorbed power for each sea state.

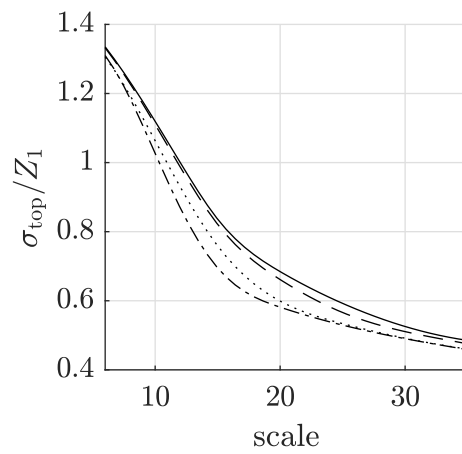


**Fig. 12.** Maximum standard deviation of the displacement of the bag top, normalised with the mean freeboard, for the four tendon elasticity cases: Case 1 (solid), Case 2 (dashed), Case 3 (dotted), and Case 4 (dash-dotted).